Magnetic Nanowire Synthesis: A Chemical Engineering Approach

Ouar Nassima, Farhat Samir, Mercone Silvana, Zighem Fatih, Schoenstein Frédéric, and Jouini Noureddine
Laboratoire des Sciences des Procédés et des Matériaux, CNRS, LSPM – UPR 3407, Université Paris 13, PRES Sorbonne-Paris-Cité, Villetaneuse, 93430, France

Hinkov Ivaylo
Dépt. de Génie Chimique, Université de Technologie Chimique et de Métallurgie, Sofia 1756, Bulgaria

Wang Guillaume and Ricolleau Christian
Laboratoire Matériaux et Phénomènes Quantiques, CNRS, UMR 7162, Université Paris Diderot, Bâtiment Condorcet, Paris, 75205, France

DOI 10.1002/aic.14605
Published online September 5, 2014 in Wiley Online Library (wileyonlinelibrary.com)

Bimetallic one-dimensional cobalt–nickel magnetic nanowires capped on both sides with conical heads were synthesized using the polyol process. Then, the process was scaled up to produce magnetic nanowires in sample aliquots of approximately 20 g. The scale-up strategy involved improving the mixing reagents using either axial or radial mixing configurations and was experimentally validated by comparing the structural and magnetic properties of the resulting nanowires. The results indicated a connection between the flow patterns and the size and shape of the nanowires. When a Rushton turbine was used, shorter nanowires with unconventional small heads were obtained. Because the demagnetizing field is strongly localized near or inside these heads, the coercive field was enhanced nearly twofold. These results were confirmed by micromagnetic simulations using isolated nanowires. In addition, the development of flow patterns at the small and pilot scales was predicted and compared using three-dimensional turbulent computational fluid dynamics simulations. © 2014 American Institute of Chemical Engineers *AIChE J*, 61: 304–316, 2015
Keywords: scale-up, nanomaterial, magnetic nanowires, computational fluid dynamics

Introduction

Anisotropic nanosized one-dimensional (1-D) magnetic nanowires have been actively investigated in an effort to utilize them as advanced materials. In contrast to their bulk behavior, the physical properties of nanowires at their characteristic length scale are strongly governed by quantum confinement effects. This enables the use of such materials in several applications, such as spintronics,[1] ultrahigh-density magnetic storage materials,[2,3] ferrofluids,[4,5] magnetic refrigeration systems,[6,7] and biomedical or catalysis applications.[8,9] The (1-D) geometry and high aspect ratio (i.e., high shape anisotropy) of nanowires enhance their coercivity and prevent them from being superparamagnetic.[10] In addition, the chemical nature of nanowires varies depending on the application, but, in all cases, the control of morphological characteristics such as size distribution,[11–13] aspect ratio and shape of the nanowire ends,[14–16] crystal structure[13,17] and composition[17–19] as well as the magnetic interaction between nanowires,[20] is essential to control the final physical properties of the material.

More specifically, high anisotropy is a prerequisite for hard magnetic properties.[10] Hence, the key issue in the fabrication of magnetic nanowires is to break the symmetry during their growth to obtain specifically 1-D objects. This could be achieved via the template route, as in the electrodeposition of magnetic metals into nanoporous membranes with a typical diameter in the range 30–500 nm and a length on the order of approximately 10 μm.[1] This method produces relatively well-aligned objects, but the individual nanowires are generally polycrystalline with a large diameter, which typically leads to a decrease in coercivity. To reduce the diameter of the nanowires, open carbon nanotubes have been suggested as ultraconfined templates to encapsulate melted metals or salts via capillarity forces.[21] However, due to the small cavity diameter of 1 to 10 nm, the filling efficiency is very low, decreasing the length of the nanowires. Owing to these disadvantages, template methods have not yet been adapted to mass production. An alternative approach is the use of liquid-phase precipitation in the so-called polyol route. This process was first developed to produce finely divided metallic powders and was patented in 1985.[22] Because of their hydrogen bonding ability and relatively high dielectric constant, polyols act as solvents that can dissolve the majority of inorganic precursors such as metallic salts. In addition, due to their chelating properties, polyols can also function as coordinating solvents, complexants, and

Correspondence concerning this article should be addressed to S. Farhat at samir.farhat@lspm.cnrs.fr.

surfactants that adsorb on the elementary particle surface during growth, preventing agglomeration. Polyols are also good reducing agents for various metals such us copper, cobalt, and nickel.[23] The polyol process has been used to produce several classes of metallic nanowires by the heterogeneous nucleation of metals such as cobalt–nickel,[24–30] silver,[31,32] platinum,[33] and gold.[34] Advances in nanowire synthesis and processing are creating both opportunities and challenges for chemical engineers, as reviewed by Korgel for semiconductor nanowires.[35]

As compared to template methods, the better compromise between the length and the diameter of the magnetic nanowires is actually offered by the Polyol process that involves liquid-phase precipitation. Since the most common type of mixed reactor used in chemical engineering is the stirred tank, scaling up this process is evidently the simplest to achieve as compared to the other methods. In stirred tanks, energy is supplied by the impeller using either axial or radial flows.[36] The quality of mixing depends on the relative distribution of mean and turbulent kinetic energy. This could be achieved by choosing the appropriate impeller configuration and by controlling the local turbulence near the impeller. More specifically, turbulent mixing and chemical reaction in baffled stirred tank was studied for different chemical systems involving a number of intermediate steps as well as parallel and serial reactions. The complex nature of reactive precipitation makes its scaling up most challenging due to the presence of primary and secondary parallel and interdependent processes such as primary nucleation, crystal growth, ageing, and agglomeration. The dependence of these processes rates on supersaturation is also highly system-specific and mixing affects the generation of supersaturation and its redistribution in the given system. For spherical magnetic nanoparticles synthesis, decreasing the size below 10 nm is needed to enhance their superparamagnetic behavior at room temperature.[37] Indeed, this characteristic is required for their biomedical applications such as contrast agents in NMR imaging and nanoheaters in hyperthermia. When performing a large scale liquid reaction in agitated vessels, it was reported that variables such as stirring rate affects nanoparticle size and polydispersity.[37–44]

In this article, we focus on a particular category of magnetic nanowires fabricated by the polyol process. Owing to its simplicity and versatility, polyol-mediated synthesis is a good candidate for industrial fabrication. Because the intrinsic morphological characteristics of nanowires are crucial for a given application, the scale-up of the process must respect the precise conditions of mixing reagents, heat transfer and mass transfer to reproduce the nucleation and growth conditions in larger reactor volumes. The majority of these rate processes are scale-dependent, and it is important to identify a reliable method to design or model larger-scale processes using information obtained from smaller processes. Although precipitation is widely used in the chemical and pharmaceutical industry, successful scale-up remains difficult due to the absence of a validated methodology that bridges the gap between the molecular and macroscopic length scales over a wide range of time scales. In the simplest case, similarity on different scales is fulfilled when dimensionless groups such as the Reynolds or Damköhler numbers have the same value at different scales. However, this equivalence is difficult to achieve for all of the dimensionless groups that characterize a given process. In these cases, a trade-off between different dimensionless groups must be made by weighting parameters according to their expected influence on the process. Scale-up then loses its theoretical base and becomes empirical.[45] An alternative approach is the mathematical modeling of the underlying physical and chemical processes in the reaction vessel using clearly and quantitatively understood mechanisms, which is not always possible. For these reasons, we developed our strategy for scaled-up nanowire synthesis in two steps. In the first step, the synthesis conditions were extrapolated empirically from the laboratory to the pilot scale and validated through *ex situ* characterizations of the obtained nanomaterials. Because solving combined computational fluid dynamics (CFD) and population balance (PB) equations remains impractical due to the lack of reliable nucleation and growth kinetics., in the second step, computationally efficient CFD calculations were performed to depict the turbulent flow patterns and energy dissipation under different axial and radial impeller geometries.

Nevertheless, if the nucleation and growth kinetics are known, coupling CFD and population balance equation (PBE) in nanoparticle and submicronic precipitation contexts become possible with the objective of the development of a predictive CFD-based models that could be used to design and scale-up precipitation operation. Such a model must accurately describe the flow and turbulence fields, the interaction between chemical reaction and turbulence, and must use accurate kinetic expressions for the different growth steps. In the case, when rapid mixing and high supersaturation are needed to provide homogeneous kinetics of precipitation, mixing become an important part of the problem. Several published works investigated the particle formation dynamics by coupling (CFD) with (PBE).[46–51]To predict particle-size distribution (PSD), these models include nucleation, growth, turbulent mixing, agglomeration etc. and the coupling between them in various types of reactors.[52–59] The Navier–Stokes fluid dynamics equations are generally solved using the Reynolds averaging approach (RANS) formulation, and mixing models were added to account for mixing at scales less than the grid resolution.[46,49] In the case of precipitation in stirred tank reactors, instead of CFD, certain models used a compartmental mixing model that required less Central Processing Unit (CPU) time but the capacity for predicting the (PSD) width is poor due to differences in mixing histories.[46] To include temporal and spatial fluctuations in the flow through the mixer, direct numerical simulation was coupled with the PB model using a Lagrangian approach.[56] Numerical methods to solve (PB-CFD) problems have been recently reviewed in the light of robustness, accuracy, and CPU time.[60]

This work presents the scaling-up strategy used to produce cobalt–nickel bimetallic nanoparticles by the polyol process in a pilot scale. The reactions were first conducted in a 0.25-liter laboratory-scale batch stirred reactor and then scaled up to a volume of 4.5 L with the aim of maintaining similar material characteristics.

The scale-up ratio defined as $\text{scale}-\text{up ratio}=\frac{\text{large}-\text{scale production rate}}{\text{small}-\text{scale production rate}}$ is usually within a range from 10 to 1000 for scale-up from laboratory scale to the pilot plant unit and within a range from 10 to 1500 for scale-up from pilot plant units to industrial plants, depending on the process and system involved.[45] In the case of CoNi nanowires studied in this work, this ratio is approximately 20. This is a lower limit of the scale-up corresponding to an academic prototype. Nevertheless, more reliable scale-up could be achieved from academic-level prototyping to industrial-level manufacturing.

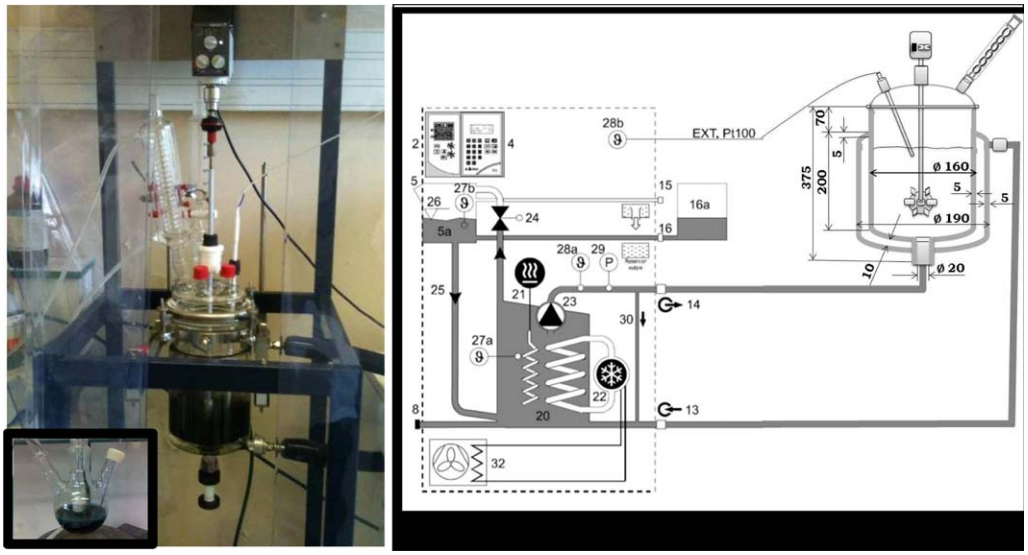

Figure 1. Photography of the pilot scale reactor with in insert the small scale reactor.

On the right is the schematic of the overall recirculating heater circuit for the pilot scale vessel. [Color figure can be viewed in the online issue, which is available at wileyonlinelibrary.com.]

Several studies have indicated that the precipitation of nanoparticles requires a high mixing intensity and that the mean particle size and the width of the PSD decrease as the mixing intensity increases.[61–66] To develop a rational design, different axial, and radial flow impellers were studied by (CFD), and the flow fields generated by these impellers were calculated for the laboratory- and pilot-scale reactors.

Experimental

Magnetic cobalt–nickel nanowires were prepared by extrapolating the stoichiometric conditions of the small-scale synthesis (Experiment E1) to the pilot scale with either axial mixing (Experiment E2) or radial mixing (Experiment E3). To vary the mixing behavior, a straight paddle and Rushton turbine were used. For all experiments, nanowires were obtained by the reduction of cobalt (II) acetate tetrahydrate 98% ($Co(C_2H_3O_2)_2.4H_2O$) and nickel (II) acetate tetrahydrate 98+% ($Co(C_2H_3O_2)_2.4H_2O$) in the presence of ruthenium (III) chloride hydrate 99.9% (PGM basis), with Ru 38% min ($RuCl_3.H_2O$) acting as the nucleating agent. The polyol was 1,2-butanediol ($C_4H_{10}O_2$), and the base was sodium hydroxide pellets PRS Codex (NaOH). All chemicals were purchased from Sigma Aldrich. For all syntheses, the molar concentrations of the metallic precursors, nucleating agent, and sodium hydroxide were 0.08, 0.0024, and 0.15 mol/L, respectively.

At the pilot scale, synthesis was achieved in a 4.5-L stirred and jacketed glass batch reactor with an internal diameter of 150 mm, a double jacket and a paddle stirrer. In addition, the external reactor surface was insulated from ambient conditions, making the reactor nearly adiabatic. Compared with the small laboratory-scale system, this configuration was designed to improve heat exchange in the reactor, thereby minimizing heat loss because the surface-area-to-volume ratio decreases with volume. In addition, due to the magnetic activity of the powder, the steel stirrer was fully encapsulated in Teflon® PTFE. The stirrer paddle was powered by a 50-watt motor (Heidolph RZR 2021) with a digital display and a speed range of 40 to 2000 rpm. As shown in Figure 1, oil was circulated through the reactor jacket from a Julabo PrestoLH40 cryo thermostat unit. The internal reactor temperature was measured using a Pt100 thermometer. This parameter was controlled using a self-optimizing controller (Intelligent Cascade Control) operating in a wide working range from 228 to 523 K to enable rapid heating and cooling as well as temperature stability.

After synthesis, samples of the obtained black magnetic powders were removed, centrifuged, washed in alcohol, and dried at 323 K. Samples were structurally characterized by X-ray diffraction (XRD) using an INEL diffractometer (ω, 2θ) with a cobalt anticathode ($\lambda = 1.7809$ Å, $\omega \sim 5°$, and 2θ ranging between 30° and 80°). The mean crystallite size was calculated from the (100) and (002) lines using Scherrer's equation,[67,68] $L_{hkl} = \frac{k\lambda}{B\cos(\theta)}$where λ is X-ray radiation wavelength ($\lambda = 1.5406$ Å), θ the Bragg's angle at which the peak is observed measured in radians, and B is the full width of diffraction line at half of the maximum intensity (FWHM. The morphology of the powder was studied by scanning JEOL2011 transmission electron microscopy (TEM) operating at 200 keV. Field emission gun scanning electron microscopy (FEGSEM) images were obtained with an accelerating voltage of 20 to 25 keV using a Zeiss Supra 40 VP microscope. Quantitative high resolution (HRTEM) analyses of a single nanowire were also performed using a JEOL JEM-ARM200F electron microscope. This microscope combines a cold field emission gun and an aberration corrector on the objective lens.[69] To determine the composition of a single nanowire, X-ray analysis in STEM mode (scanning transmission electron microscopy/energy dispersive X-ray STEM-EDX) was implemented. The X-ray signals resulting from the interaction of the primary electron beam with the nanowires were analyzed using a JEOL energy-dispersive X-ray analyzer (EX-24063JGT). To obtain an adequate signal-to-noise ratio for meaningful analysis, the EDX spectra were acquired with the largest spot size available (spot 1C), and the acquisition time was set to 100 s. Finally, the magnetic properties of $Co_{80}Ni_{20}$ were measured using a MPMS 3 Quantum Design system capable of applying a magnetic field ranging from −70 kOe to +70 kOe at room temperature (300 K) and cooled temperature (4 K).

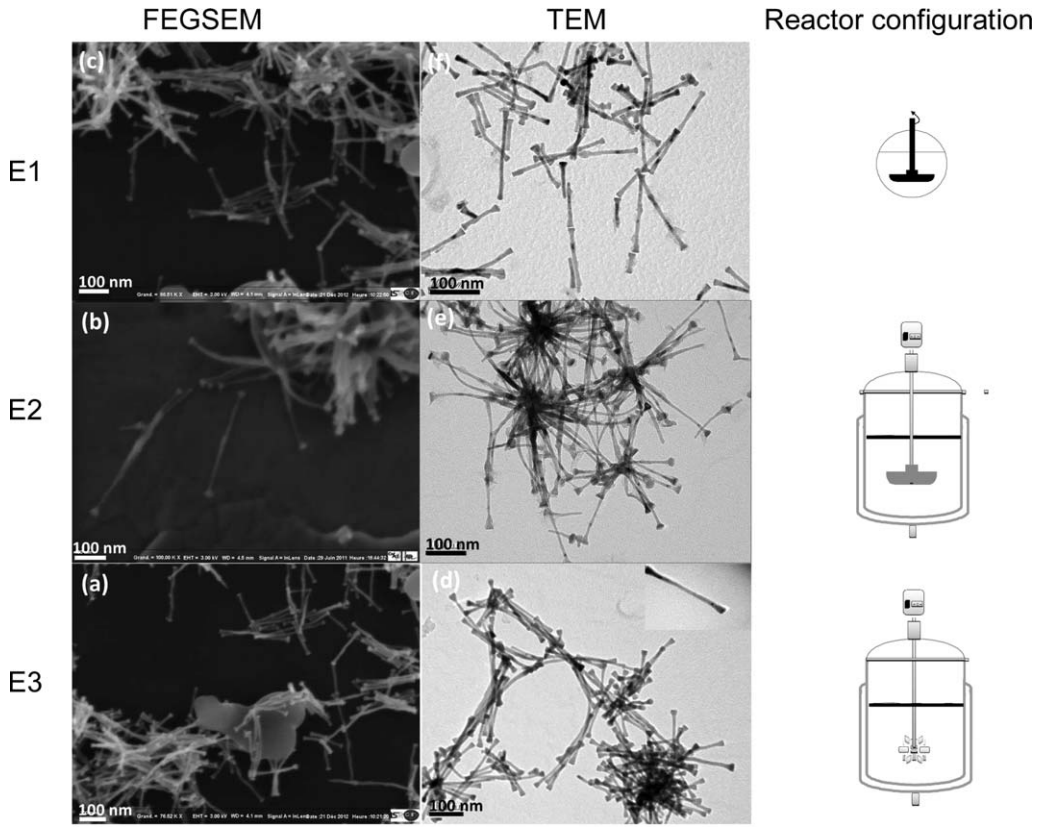

Figure 2. FEGSEM (left) and TEM (right) micrographs for the small scale reactor sample E1, large scale with axial (sample E2), and radial (sample E3) mixing.

Results and Discussion

Small-vs. pilot-scale synthesis

As a first step, the development of the large-scale reactor was based on determining the effect of the most important process parameters on the nanowires shape and size distribution from the analysis of laboratory-scale data. The parameters affecting the anisotropy are found to be the elemental Co/Ni composition, the nucleation molar ratio $\frac{[Ru]}{[Co+Ni]}$, and the sodium hydroxide concentration leading to different morphologies varying from spheres to nanowires. According to Ung et al.,[10] the morphology of the CoNi nanomaterials was mainly determined by the relative rates of nucleation and growth during heterogeneous nucleation in polyols. A lower nucleation rate and higher growth rate favored the formation of anisotropic shape such as rods and wires. A higher nucleation rate favored the formation of isotropic shapes such as spherical particles and platelets.

From parametric study, chemical reactions appear to be the rate-determining step in the polyol process. Hence, the reactor volume is likely to be crucial for scale-up. Once the geometry of the small- and pilot-scale reactors defined, we considered as a first approach equal stirring rate from scale to scale as scale up criteria and we varied the mixing configuration from radial to axial in the pilot-scale reactor. This choice is justified by the low scale-up criteria of approximately 20 used in this study. For higher volume reactors, equal power input per unit mass, equal local near the impeller power dissipation rate or equal tip speed was already proposed in the literature for other precipitation systems to ensure the same macromixing efficiency. For given reactor, impeller and baffles geometries power input P0 and power input per unit mass ε can be obtained from simple dimensional analysis using Reynolds Re and Froude Fr numbers. $P0 = f(Re,\ Fr)$. Froude number defines the ratio between inertial and gravity forces. High Fr number predicts vortices formation. In the case of the baffled reactors, the effect of the Froude number Fr can be ignored and the former relationship could be simplified to $P0 = f(Re)$ that could be determined experimentally over a range of stirrer speeds. However, as different types of impeller produce different flow fields, the flow characteristics in a vessel may vary considerably. In addition, the shear rate distribution, and therefore, the local energy distribution, changes with scale-up. With larger scales, the maximum shear rate in the impeller zone increases while the average shear rate in this zone decreases. Therefore, even when scaling up with constant power input per unit volume, the flow field looks different for different scales of operation leading to a different flow pattern, and therefore, different mesomixing and macromixing in the reactor. Scale-up with a constant Reynolds number leads to different local Damköhler numbers, and therefore, different reaction and precipitation rates, whereas Qian et al.[70] observed that scale-up with constant tip speed of the impeller leads to equal nucleation rates on different scales. In addition, for processes with heat transfer limitation, the surface-to-volume ratio could have a significant impact on the outcome of the scale-up study.[71]

The results of the analysis of powders E1 to E3 by FEGSEM and TEM are shown in Figure 2. The morphology of the nanowires was characterized by long, straight, 1-D objects at both the small and pilot scales, suggesting a successful scaling up. By focusing the beam of the microscope on a single nanowire, we were able to accurately determine

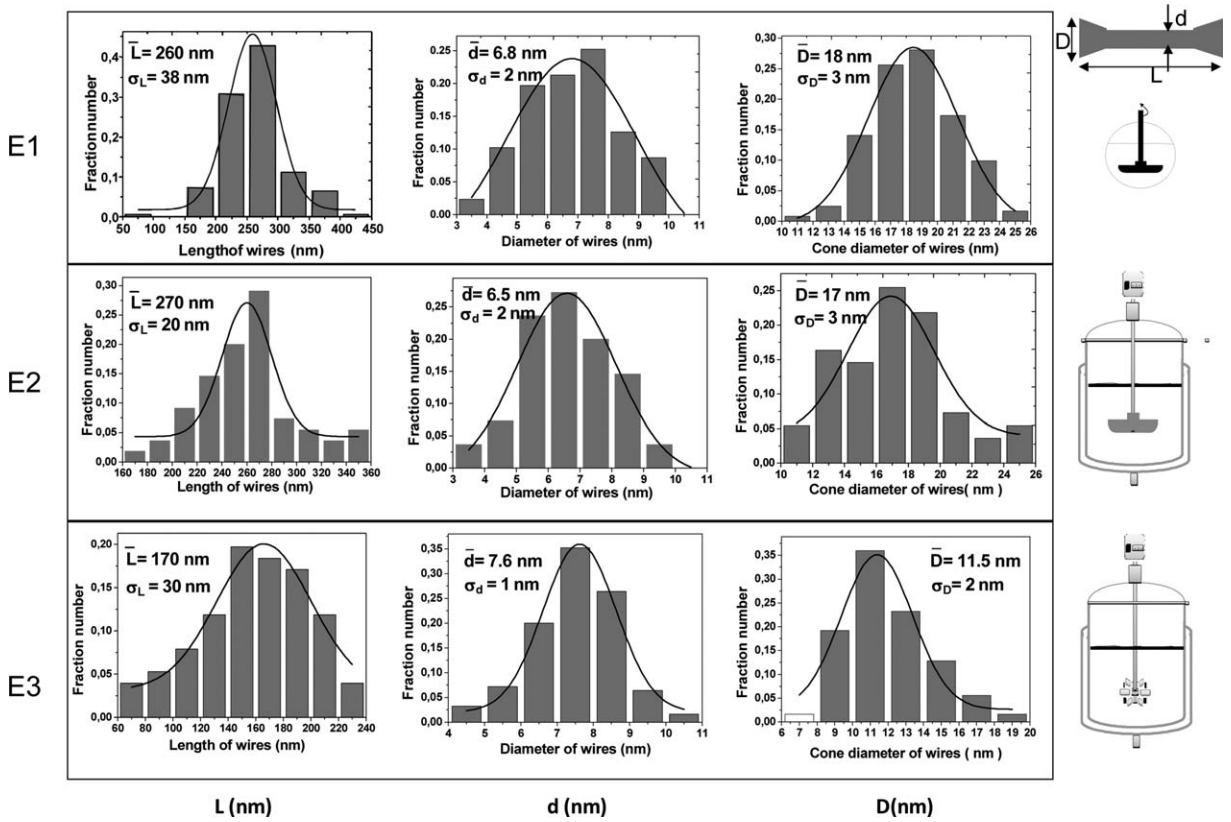

Figure 3. Nanowire size and shape distribution for the small scale reactor E1, large scale with axial (E2), and radial (E3) mixing.

***L* and *d* are the nanowire length and diameter and *D* is the head diameter at the both ends of each nanowire. The over bar and σ indicates the average values and standard deviation of each variable, respectively.**

its individual length L and diameter d. Moreover, each nanowire was terminated at both ends by a cone-shaped structure with diameter D. EDX measurements performed on these nanowires revealed that the core of the nanowire was rich in cobalt, whereas the conical heads were rich in nickel.[72,73] These results were confirmed by electron energy loss spectroscopy (EELS).[25,74]

As previously reported by Ung et al.,[10] cobalt nickel nanowire formation occur by progressive dissolution of the solid precursor followed by reduction of the dissolved species by the polyol itself and subsequent nucleation and growth of the metal particles from the solution as represented by the reaction (r1).

$$(\mathrm{CoII+NiII})\ \text{solid phase} \leftrightarrow \left(\mathrm{Co^{2+}+Ni^{2+}}\right)\ \text{solution} \rightarrow \mathrm{Co0+Ni0} \qquad \text{(r1)}$$

Indeed, the polyol in excess in the solution have sufficient reducing power to reduce both cobalt and nickel. Nevertheless, since the standard redox potential of Co^{2+}/Co is lower than Ni^{2+}/Ni, cobalt ions are reduced first explaining why the central column involves mainly the cobalt. After consumption of all the cobalt, the caps are progressively formed mainly by the residual nickel in the solution.

Micromagnetic simulations performed by Ott et al.[75] on capped cobalt-based magnetic nanowires with various head shapes demonstrated the negative effects of these heads: they act as nucleation points for magnetization reversal, leading to a decrease in coercivity for capped nanowires compared with perfectly cylindrical nanowires. Figure 3 plots the statistical distributions of L, d, and D obtained from the TEM images. The statistics on characteristic sizes (L,d,D) was performed on at least 100 nanowires from several TEM images issued from the same synthesis. The products obtained in E1 and E2 were similar, with an average diameter of approximately 7 nm and a length of approximately 260 nm. However, when the Rushton turbine was used, shorter ($\sim$170 nm) and thicker ($\sim$7.6 nm) nanowires were obtained, suggesting a relationship between the growth reaction and mixing in specific cobalt–nickel nanowire synthesis.

The structure of an individual nanowire was investigated by HRTEM (Figure 4) to further characterize the nanowire morphology and crystal structure. For the E2 sample, the diameter of the nanowires was estimated by HRTEM to be approximately 6 nm, which is consistent with the results obtained by FEGSEM and TEM. The magnified view of an individual nanowire revealed perfect single crystalline zones within the nanowire body, with a preferred growth direction along the c axis. The power spectrum of the image obtained from Fourier transform analysis and inserted in Figure 4a demonstrates the single crystalline nature of the CoNi materials. Some stacking faults regularly spaced along the revolution axis of the nanowire were also observed. The crystallographic c axis was parallel to the stacking direction, and the CoNi nanomaterials grew anisotropically along the (100) plane, which was confirmed by the XRD pattern. When viewed along the (010) direction (Figure 4b), the lattice spaces of 0.210 nm were ascribed to the (100) planes of the hexagonal close-packed (hcp) Co phase. In Figure 4b, the presence of a thin CoO layer followed by a disordered organic phase is also apparent, most likely due to adsorbed

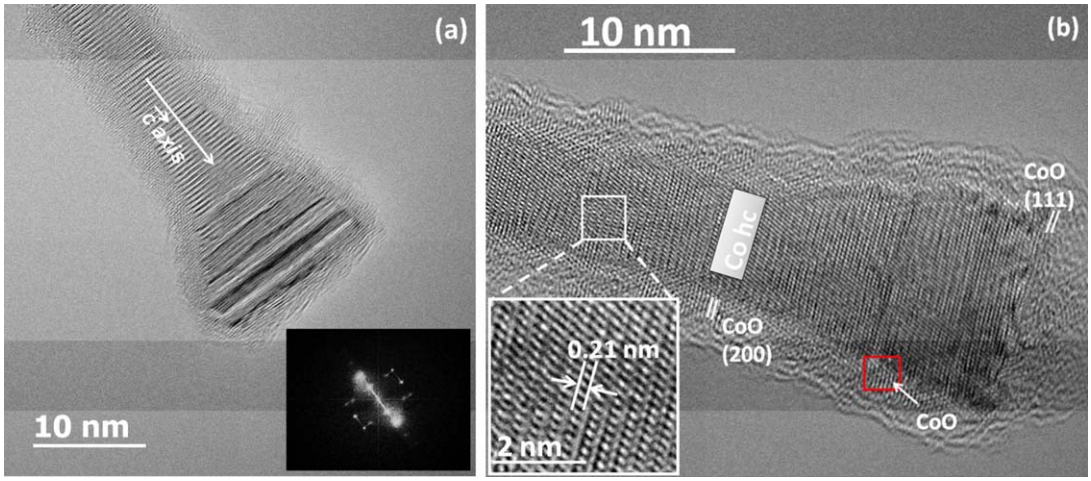

Figure 4. High resolution TEM images of bimetallic $Co_{80}Ni_{20}$ nanowire obtained in the pilot scale (E2).

Individual nanowire with the *c* axis. The insert is a selected area power spectrum of the image obtained from Fourier (a), HRTEM image of the cobalt–nickel wire showing a magnification of the local structure of the Co body surrounded by a CoO shell (b). [Color figure can be viewed in the online issue, which is available at wileyonlinelibrary.com.]

polyol molecules at the external surface of the nanowires. These features confirm previous results obtained in laboratory-scale experiments.[25–28,72]

EDX quantification of the cobalt-to-nickel ratio was performed at two positions on the nanowires obtained at the pilot scale (E2), and the results are plotted in Figure 5. From these results, we can conclude that the core of the nanowire (position a) is poor in nickel, whereas the conical head (position b) contains many more nickel atoms. This result confirms our previous EDX quantification performed at the laboratory scale[64,65] and the EELS measurements.[25,73]

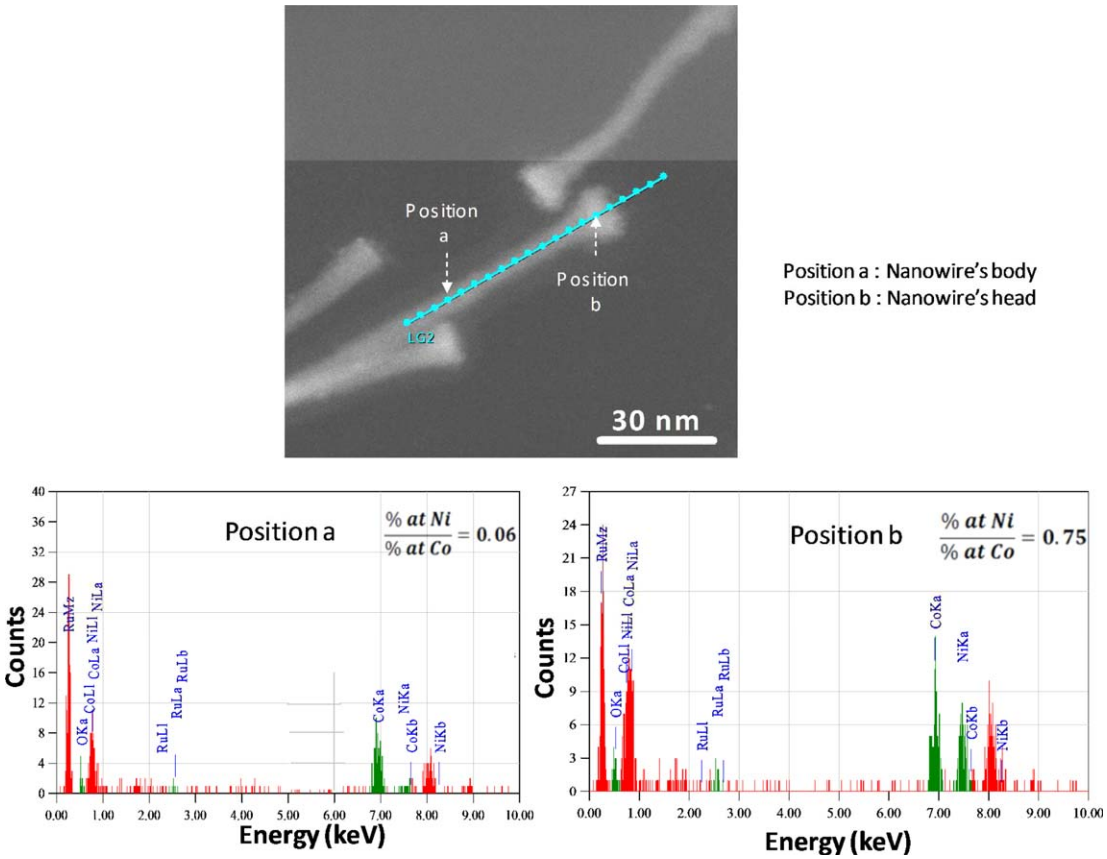

Figure 5. EDX quantification of cobalt vs. nickel ratio in two positions of the nanowires obtained in the pilot scale (E2).

As shown in the TEM image, position "a" is related to the core of the nanowire and position "b" is the head. [Color figure can be viewed in the online issue, which is available at wileyonlinelibrary.com.]

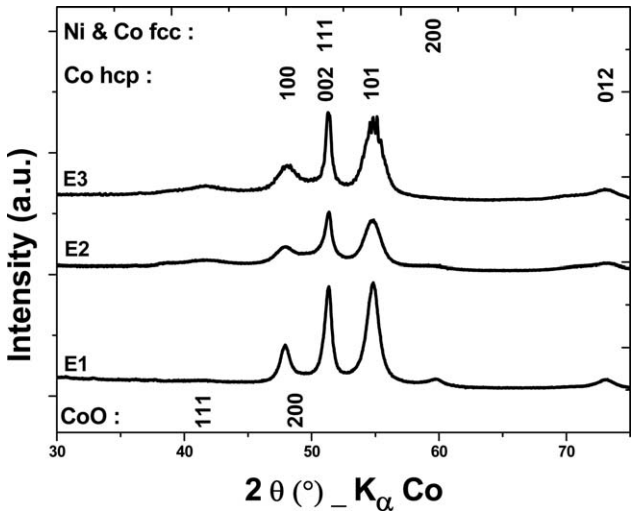

Figure 6. XRD pattern of $Co_{80}Ni_{20}$ obtained in E1, E2, and E3 samples.

Positions of the cobalt, nickel, and cobalt oxide peaks are indexed.

To further characterize the structure of the nanowires, we performed XRD analysis on the three samples. The nanocrystallite sizes have been calculated using the Scherrer's equation based on the assessment of the broadening of XRD peaks. Generally the Scherrer formula provides a lower bound on the particle size due to dislocations, stacking faults, and grain boundaries. For isolated nanoparticles, the use of Scherrer equation for measuring crystallite size is limited by uncertainty of the Scherrer constant (k) due to the presence of polydisperse particles. The presence of polycrystalline particles may also lead to inaccurate particle size estimation by Scherrer equation, given that crystallite and particle sizes are not equivalent.The XRD patterns are shown in Figure 6: the lines are broadened, suggesting the formation of nanocrystalline phases. More specifically, the line (002) is a signature of anisotropic objects with growth along the crystallographic *c* axis of the cobalt hcp phase. The full width of both lines (100) and (002), which are respectively perpendicular and parallel to the *c* axis of the hexagonal phase, were used to calculate the average crystallite size using Scherrer's method. The results are summarized in Table 1. The average value of the crystallite size assigned to plane (100) is close to the diameter of the rods measured by TEM. However, the average length determined by TEM and $L_{(002)}$ estimated by XRD differ greatly due to the presence of the stacking faults revealed by HRTEM. The origin of this difference could be attributed to the nanowire growth mechanism by ''oriented attachment,'' where small CoNi nanoparticles with common crystallographic orientations directly combine together by magnetic attachment to form larger ones. Evidently, the uncertainty on L002 exists, yet it is not crucial for the total shape anisotropy of the nanowire. The three nanopowders contain both hcp and face-centered cubic (fcc) phases. The relative percentages of the phases were calculated by Match software[76] and are presented in Table 1. The hcp phase was the dominant phase and is attributable to cobalt, whereas the fcc pattern may be attributable to a mixture of cobalt and nickel or to a solid solution of these two elements.[72] The XRD data also confirmed the minor phase of cobalt oxide (CoO) previously observed in the HRTEM micrographs. The structural properties of the nanowires obtained from the XRD data at the small and large scale are similar, confirming a successful scale-up.

Table 1. XRD vs. TEM Structural Analysis of the Bimetallic $Co_{80}Ni_{20}$ Nanowires Obtained for the Small Scale Reactor E1, Large Scale with Axial (E2), and Radial (E3) Mixing

Sample		E1	E2	E3
Particle size	d_{TEM} (nm)	6.8	6.5	7.6
	$L_{(100)}$ (nm)	8.1	7.8	7.2
	L_{TEM} (nm)	260	270	170
	$L_{(002)}$ (nm)	20	21	23
Phase composition	wt. % fcc	30	27	28
	wt. % hcp	69	70	70
	wt. % CoO	1	3	2

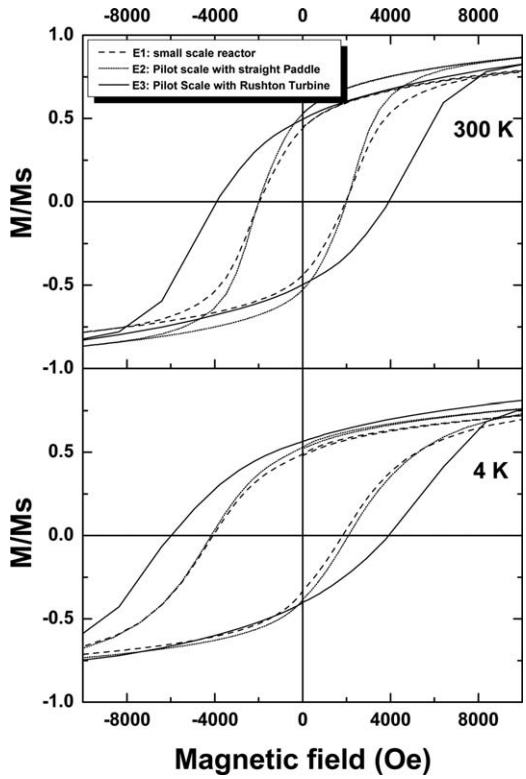

Figure 7. Hysteresis loops of the $Co_{80}Ni_{20}$ powder synthesis with E1, E2, and E3 configurations at 300 and 4 K.

Finally, to compare the magnetic performances of the samples, magnetization curves were recorded by a VSM-SQUID Quantum Design standard system at 300 and 4 K (Figure 7). All samples clearly exhibited ferromagnetic behavior characterized by saturation magnetization (*Ms*), remanent magnetization (*Mr*) and the coercive field (*Hc*), which are listed in Table 2.

From Figure 7 and Table 2, it can be concluded that all three samples (E1, E2, and E3) exhibit a typical magnetic signature characterized by an open cycle (hysteresis loops), a non-negligible coercive field and remanent magnetization of the same order of magnitude at 300 K. This result suggests that, from a magnetic perspective, the scale-up was successful. Indeed, when a straight paddle was used, the extracted coercive fields at 300 and 4 K ($Hc = 2065$ Oe and $Hc = 3126$) of sample E2 (pilot scale) were very close to the fields ($Hc = 1970$ Oe and $Hc = 2946$ Oe) of sample E1

Table 2. Experimental (top) vs. Numerical (bottom) Magnetic Properties of the $Co_{80}Ni_{20}$ Nanowires Synthesized with E1, E2, and E3 Reactors and Measured at 300 and 4 K

Experimental Results						
	E1		E2		E3	
	4 (K)	300 (K)	4 (K)	300 (K)	4 (K)	300 (K)
He (Oe)	−1124	16	−1032	35	−1010	4
Hc (Oe)	2946	1970	3126	2065	4920	3922
Mr (emu/g)	19	14	28	20	54	38
Ms (emu/g)	39	32	53	38	97	77
Mr/Ms	0.46	0.43	0.49	0.52	0.53	0.49

Numerical Results			
	E1n	E2n	E3n
L (nm)	260	270	170
D (nm)	18	17	12
t (nm)	9	9	6
d (nm)	6.8	6.5	7.6
Mr/Ms	∼0.92	∼0.93	∼1
Hc (Oe)	1940	2070	3100

The geometrical dimensions considered during the micromagnetic simulations are given with the deduced remanent magnetization and coercive field. Hc: Coercivity field in Oersted (Oe) - He: Exchange bias (Oe) - Mr/Ms: Remanence to saturation magnetization ratio.

(small reactor). Moreover, as shown in Figure 4, during nanowire drying, an oxide nanoshell (CoO particles) was formed. As this shell is certainly in an antiferromagnetic state at 4 K, an exchange interaction between the ferromagnetic core and the antiferromagnetic shell occurs.[75] In the three samples, this effect resulted in a dissymmetry of the hysteresis cycles, which was quantified through the measurement of the so-called exchange bias field (*He*). Indeed, the exchange bias field can present complex behavior that depends on many factors, such as the oxide shell thickness and the magnetic history of the sample.[75,77]

However, the geometry of the mixing paddle has an effect on the coercive field *Hc*. Indeed, when a Rushton turbine (E3) was used, the coercive field was significantly increased to $Hc = 3922$ Oe and 4920 Oe at 300 and 4 K, respectively. This elevated coercive field is mainly due to the weaker diameter of the nanowire heads obtained with the Rushton turbine, as shown in Figures 2 and 3. The quality of the reagent mixture during the synthesis of cobalt nickel nanowires is believed to influence their growth mechanism. To our knowledge, this result has not been reported previously. To understand these experimental observations, micromagnetic simulations on isolated nanowires were performed using the NMAG micromagnetic package.[77,78] Thus, three different nanowire geometries (called E1n, E2n, and E3n) were considered; their geometrical dimensions (reported in Table 2) were defined based on the mean experimental values obtained during SEM and TEM analysis of the three different samples (E1, E2, and E3, respectively). The magnetic parameters of bulk $Co_{80}Ni_{20}$ were used during the simulations: magnetization saturation $Ms = 1.2 \times 10^3$ emu·cm^{-3} and exchange stiffness $A = 1.0 \times 10^{-6}$ erg cm^{-1}. No magnetocrystalline anisotropy was included to avoid mixing different sources of coercivity.

Figure 8a presents the calculated magnetization curves along the revolution axis of the different nanowires. Hysteresis cycles were obtained for the three cases. The cycles of the E1n and E2n nanowires are quasi-superimposed and exhibited a linear dependence on the remanent state and the coercive field, whereas for the E3n nanowire, the cycle is nearly square. The linear dependences are the result of nonuniform magnetic moment distributions. Furthermore, the E3n nanowire coercive field is larger ($Hc \sim 3100$ Oe) than those of the E1n and E2n nanowires ($Hc \sim 1940$ Oe and 2070 Oe, respectively). Thus, it can be concluded that the lower experimental *Hc* values obtained for the E1 and E2 samples are due to their larger heads (diameter of the nanowires' conic heads). In this type of nanowire, the demagnetizing field is strongly nonhomogeneous and is localized near or inside the heads.[73,79] Thus, the larger heads of the E1n and E2n nanowires act as nucleation points for the magnetization reversal, and a lower applied magnetic field is required to reverse the magnetization (i.e., a lower coercive field). Figure 8b presents the magnetic moment distributions inside the different simulated nanowires at zero applied magnetic field (remanent state). The magnetization is uniform inside the E3n nanowire and nonuniform (particularly at the heads) inside the E1n (and E2n, which is not shown) nanowires. Finally, the slight difference in the calculated coercive fields for the E1n and E2n nanowires (Hc is equal to 1940 Oe and 2070 Oe, respectively) is due to the small difference in the nanowires' internal diameters (*d* is slightly larger for the E1n nanowire).[56,70] These micromagnetic simulations

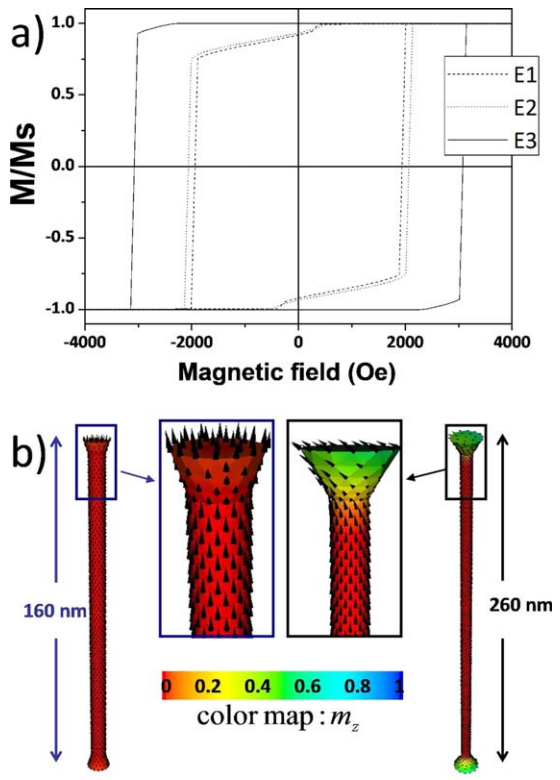

Figure 8. Micromagnetic simulation.

Magnetization curves calculated for the three different nanowires: E1n, E2n, and E3n, respectively. The magnetic field was applied along the revolution axis of each nanowire (a), Magnetic moments distributions inside the nanowires E3n (right) and E1n (left) at remanence. Colors encode m_z component of the magnetization (along the revolution axis). Zoom-in of each nanowire head is also presented (b). [Color figure can be viewed in the online issue, which is available at wileyonlinelibrary.com.]

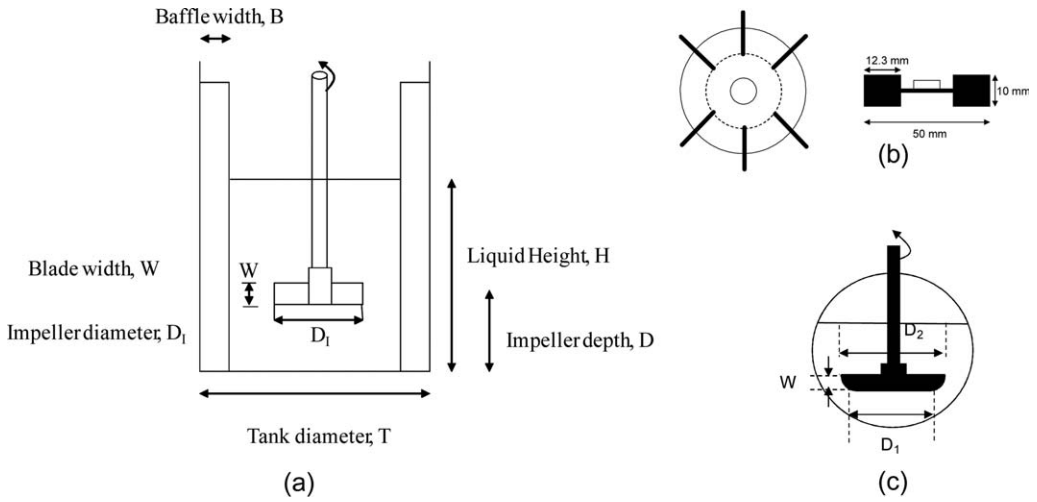

Figure 9. Simplified geometry used in CFD simulation.

Pilot scale reactor with straight paddle (a), Rushton turbine (b), and Laboratory scale spherical reactor (c).

and the experimental results are consistent, which strongly confirms that scale-up does not alter the specific magnetic behavior of such nanowires. To study the interaction between the bulk liquid phase flow and the tank and paddle geometries, we developed a CFD model, as described in the next section.

CFD modeling

To evaluate the small- and pilot-scale designs, CFD calculations were performed in a 3-D turbulent fluid flow configuration for different types of agitators and solved using ANSYS FLUENT commercial software.[80] This enabled the evaluation of alternative designs and the selection of an optimum mixing configuration. The fluid around the rotating impeller blades interacts with the stationary baffles and generates a complex, 3-D turbulent flow. Other parameters, such as the impeller clearance from the tank bottom, proximity of the vessel walls, and baffle length, also affect the generated flow. The geometry of the laboratory- and pilot-scale reactors used in this simulation are depicted schematically in Figure 9, with the appropriate geometrical parameters listed in Table 3. For the laboratory-scale reactor, a spherical tank with a diameter of $D_T = 82$ mm and a straight paddle was considered. For the pilot-scale reactor, a flat-bottom cylindrical tank with diameter $D_T = 150$ mm and baffles was used. In all simulations, the working fluid was 1,2-butanediol, which exhibits temperature-dependent viscosity and mass density, as shown in Figure 10. To simulate the synthesis conditions, a volume of 0.2 L of 1,2-butanediol was used for E1 and 2.65 L for E2 and E3. This corresponds to a total liquid height of $H = 67$ mm for the laboratory-scale reactor and $H = D_T = 150$ mm for the pilot-scale reactor. When the reactor volume was increased, four equally spaced baffles with width B = 16 mm and thickness 5.1 mm were placed on the pilot-scale tank wall to avoid vortex formation and improve the mixing efficiency.

Table 3. Geometric Characteristics of the Mixing Systems

	Laboratory Scale, E1 (mm)	Pilot Scale with Straight Paddle, E2 (mm)	Pilot Scale with Rushton Turbine, E3 (mm)
Impeller diameter	$D_1 = 50$ $D_2 = 70$	$D_I = 96$	$D_I = D_T/3 = 50$
Height of the blade	$W = 10$	$W = 30$	$W = 10$
Impeller depth	$D = 30$	$D = 50$	$D = 50$

The 3-D geometry of the reactor/paddle systems was created using ANSYS Design Modeller, and the mesh was generated by the ANSYS Meshing application, as shown in Figure 11a. In particular, the impeller region was further refined to better capture the associated flow phenomena. The impeller rotation was modelled using the multiple reference frame approach, in which the computational grid comprised two meshes: an inner cylindrical rotating volume enclosing the impeller and an outer stationary volume forming the rest of the reactor, including the baffles. The two volumes were separated by an interface. The interface was defined as an imaginary section to provide the interaction between the rotating and stationary frame. An unstructured, nonuniform tetrahedral mesh was generated inside the computational domain. Even though regular hexahedrals grid is preferable to irregular one, uniformly distributed hexahedral cells within the full 360° geometry was difficult to obtain scarifying some geometrical details of the paddles. To get a more accurate description of the impeller, the grid used in the impeller region was dandified. In addition, a grid sensitivity study was performed prior to the final grid selection using three different meshes: coarse, intermediate, and fine. It was

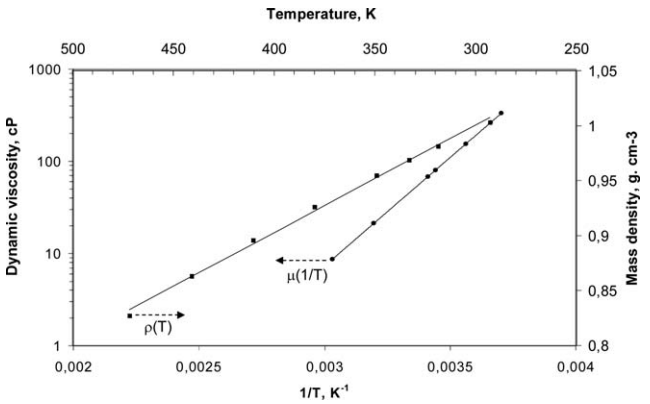

Figure 10. Dynamic viscosity μ and mass density ρ of 1,2-butanediol as a function of temperature.

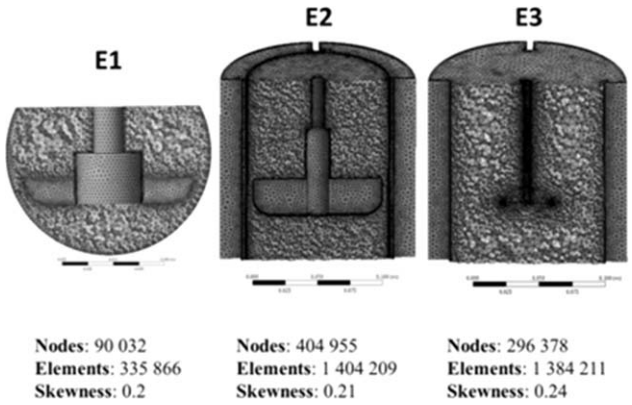

Figure 11. Computational domains.

Generated meshes in small scale reactor E1, large scale with axial (E2), and radial (E3) mixing. The final number of nodes, elements, and the skewness are given in the legend.

found that a domain consisting of 335, 1404, and 1384 k cells yielded a grid independent solution for E1, E2, and E3 simulation, respectively. This provides a computational grid sufficiently fine to resolve the problem within a reasonable CPU time, between 2 and 10 h on a four parallel processing computer.

The hydrodynamic structure of the turbulent flow in the three situations discussed above was then simulated using a 3-D turbulent model. This model uses a fully conservative finite volume method for the solution of the continuity and momentum equations, including turbulence. The governing equations are given in a Reynolds-averaged form of the Navier–Stokes (RANS) equations. When the large-scale reactor was used, the governing equations in the flow region surrounding the impeller were modified for the rotating frame. In steady RANS, turbulence models are used to resolve the time-averaged velocity and model the velocity fluctuations. The selection of the turbulence approach is critical to fully resolving the fundamentals of the mixing behavior. For solving the Reynolds stresses, the standard k-ε model with enhanced wall treatment was used. This model assumes that the normal stresses are roughly equal and are adequately represented by the turbulent kinetic energy. The following model constants were used in our simulations: $C_{1\varepsilon} = 1.44$; $C_{2\varepsilon} = 1.92$; $C_{\mu} = 0.09$; $\sigma_k = 1.0$, and $\sigma_{\varepsilon} = 1.3$. For initial and boundary conditions, the cylindrical wall, bottom wall, and baffles were modelled as stationary, impermeable walls. On these walls, a no-slip condition was applied for the liquid. The impeller shaft and hub or discs, in the case of the Rushton turbine, were specified as moving walls with an angular velocity corresponding to the impeller rotational speed. A free surface boundary condition was defined at the liquid surface. An operating pressure of 1.013×10^5 Pa was set at the liquid surface on the top of the tank. As a first approximation, only the pure solvent 1,2-butanediol was considered, with a temperature-dependent mass density ρ and dynamic

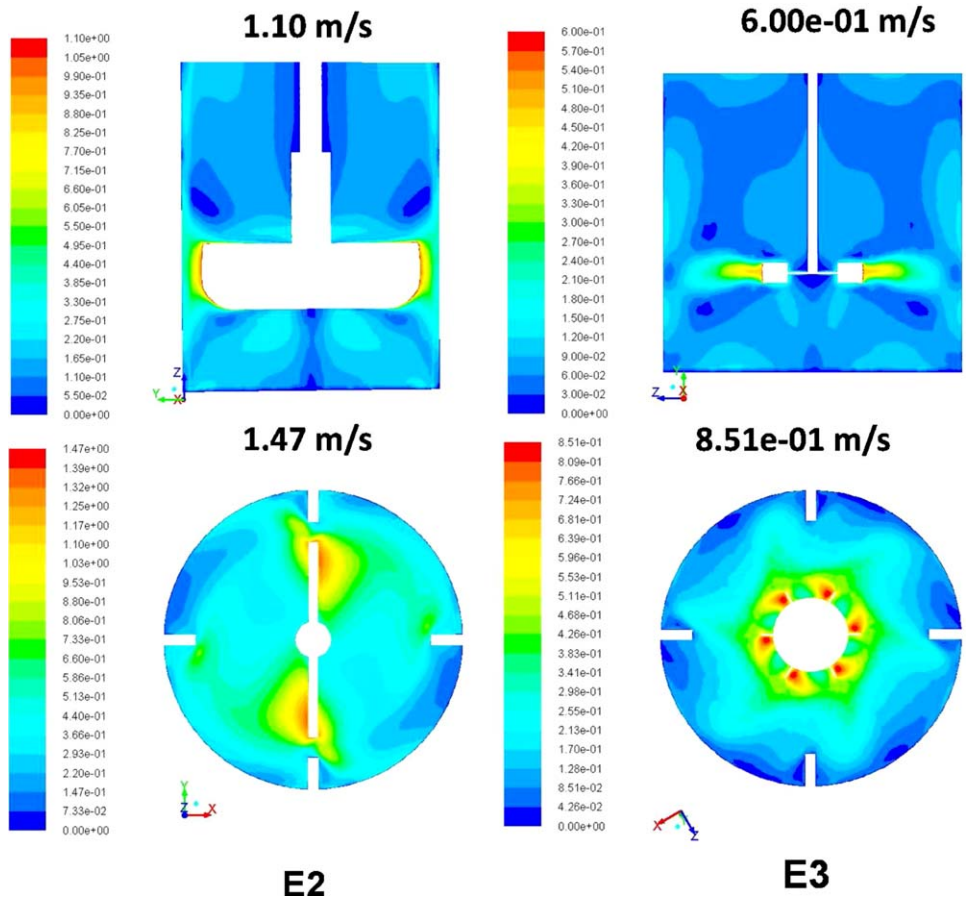

Figure 12. Velocity magnitude in m s^{-1} depicting the flow features in a vertical (up) and horizontal (down) planes in large scale with axial (E2) and Rushton turbine radial mixing (E3).

Conditions are 1,2 Butanediol as solvent, $N = 220$ RPM and $T = 438$ K. [Color figure can be viewed in the online issue, which is available at wileyonlinelibrary.com.]

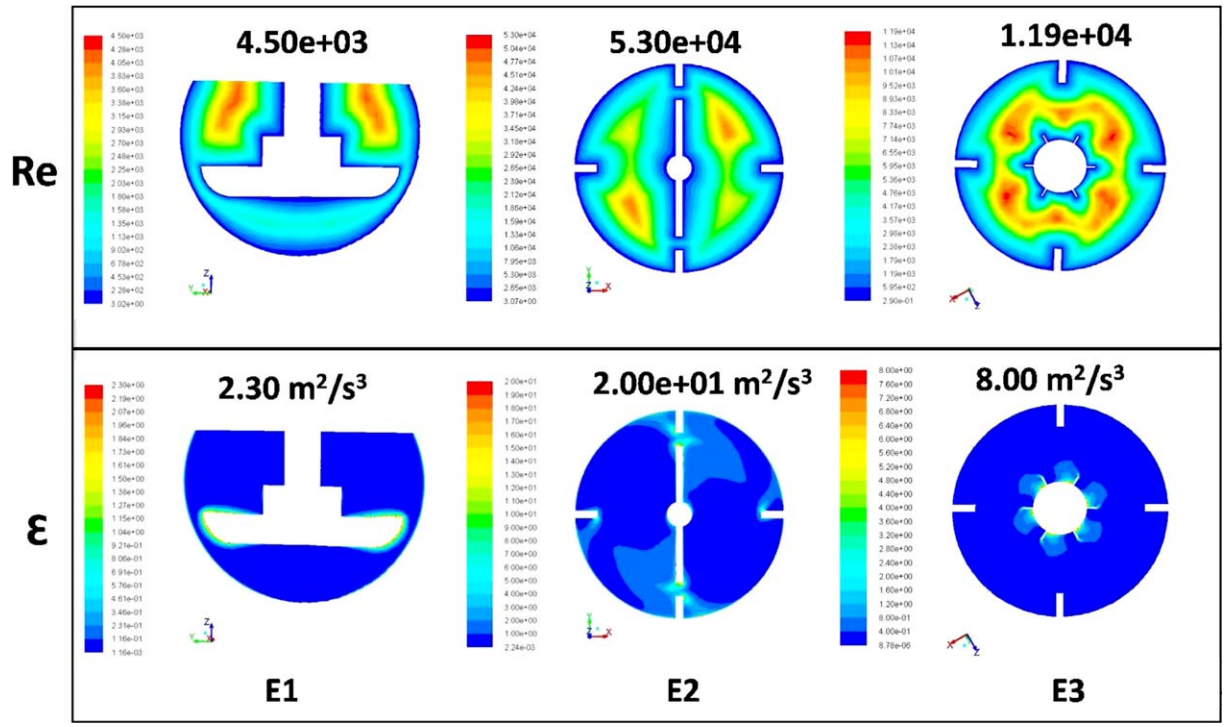

Figure 13. Contours of Reynolds numbers and Contours of predicted turbulent dissipation rate (ε) in a vertical (up) and horizontal (down) planes in large scale with axial (E2) and Rushton turbine radial mixing (E3).

Conditions are 1,2 Butanediol as solvent, $N = 220$ RPM and $T = 438$ K. [Color figure can be viewed in the online issue, which is available at wileyonlinelibrary.com.]

viscosity μ as shown in Figure 10. The impeller shaft and gravity acceleration were defined along the vertical axis. The impeller rotating speed was set to 220 rpm in all cases. The flow field was calculated using a steady-state assumption. Velocity-pressure coupling was achieved using the SIMPLE algorithm to iteratively solve the discretized equations. A first-order upwind discretization scheme was adopted for pressure interpolation and the convective term of momentum and turbulent kinetic energy. The solution residuals for all conservation equations were set to a value of 5×10^{-05}.

The discretized conservation equations were solved in the full 360° geometry for stirred tanks E1 to E3. Figure 12 gives the velocity magnitude obtained by the simulation of E2 and E3 experiments. As shown in Figure 12, the flow patterns in reactors E2 and E3 are axial-and radial-like, respectively. The tip velocity of the paddle is 1.1 and 0.8 m/s, respectively, with a better distribution of the velocity magnitude in the plane of the Rushton turbine, as shown in the cross sections at the bottom of Figure 12.

Then, we solved CFD equations for the three reactors at the same temperature 438 K and the same stirring rate $N = 220$ RPM. When the Rushton turbine was used, larger turbulent *Re* contours were obtained near the paddle (see Figure 13). Maximum *Re* numbers were always obtained near the blade tips. A comparison of the Reynolds numbers obtained from the Fluent calculations and the tank Reynolds number obtained with $\mathrm{Re} = \frac{\rho N D^2}{\mu}$ revealed a good agreement in trends.

Characteristic distributions of the rate of dissipation of the turbulence energy ε are also given in Figure 13, which indicates high and low levels of ε near and away from the impeller region, respectively. The calculated values of ε were highest near the Rushton turbine tips and the region dominated by the trailing vortices. Over most of the remaining vessel volume, ε was lower by approximately two orders of magnitude. This suggests that the reaction occurs very close to the impeller. Indeed, it is generally admitted that mixing is initiated at the macroscale level and proceeds in a cascade-like manner down to the microscale level. However, chemical reactions can only take place when the reacting species come into contact at the microscale level defined by elementary eddies in the fluid and characterized by the Kolmogorov length scale. We can qualitatively conclude that a higher and more spatially homogenous dissipated energy produces shorter nanowires and heads.

Two important parameters appear to affect the nanowire size distribution: the flow rates of reagents or the Reynolds number (*Re*) and the energy dissipation (ε). Increasing both of these parameters can reduce the particle size and decrease the distribution width, as supported by experimental and theoretical estimations of macroscale and microscale mixing.[52]

Conclusions

The polyol process is a bottom-up assembly process that is powerful for creating engineered identical structures with atomic precision and few defects. Using basic chemical engineering concepts, we demonstrated that it is possible to reproduce at a larger scale the auspicious conditions for the reduction of metallic salts in polyols. The resulting magnetic cobalt–nickel nanowires were produced in sample aliquots of tens of grams. This quantity is useful to elaborate relatively homogenous macroscopic nanostructured samples produced from the same batch synthesis by spark plasma sintering, as demonstrated in our previous works.[72,74] Nevertheless, the high viscosity and low diffusion coefficients of metallic ions

in polyols negatively affect mass transport and reaction kinetics. To avoid these negative effects, mixing systems must be optimized to facilitate the reactions by optimizing the local dissipated energy. Consequently, it is possible to control local synthesis conditions by simply choosing the appropriate mixing system for a given reactor geometry to obtain the desired size and shape of the nanowires. When a six-bladed Rushton turbine was used, shorter nanowires with unconventional small conical-shaped heads and a higher coercive field were obtained, confirming a strong relationship between flow patterns and nanowire growth. As performed in this article, CFD calculations facilitate the depiction of turbulent flow patterns and energy dissipation under different impeller geometries, providing a better picture of the mixing efficiency in the reaction vessel. Indeed, mixing, which results in bulk movement of the fluid, plays a significant role in maintaining the homogeneity of a given reaction system and in heat transfer In the context of large-size reactors, good mixing is particularly important because it is essential to maintain the same rate of mass transfer in the overall reaction medium, thereby ensuring uniformly sized and shaped nanoparticles. Work is in progress to improve the spatial uniformity of the energy dissipation rate by using draft tubes during nanowire synthesis by the polyol process.

Acknowledgments

IFR Paris Nord Plaine de France (PPF) as well as ANR (Agence Nationale de la Recherche) and CGI (Commissariat à l'Investissement d'Avenir) are gratefully acknowledged for their financial support of this work through Labex SEAM (Science and Engineering for Advanced Materials and devices) ANR 11 LABX 086, ANR 11 IDEX 05 02." The VSM-SQUID for magnetic static measurements at LPEM (ESPCI-ParisTech) has been supported through grants from the Ile-de-France regional counsel.

Literature Cited

1. Fert A, Piraux L. Magnetic nanowires. *J Magn Magn Mater*. 1999; 200(1–3):338–358.
2. Yu CY, Yu YL, Sun HY, Xu T, Li XH, Li W, Gao ZS, Zhang XY. Enhancement of the coercivity of electrodeposited nickel nanowire arrays. *Mater Lett*. 2007;61:1859–1862.
3. Liu L, Li H, Fan S, Gu J, Li Y, Sun H. Fabrication and magnetic properties of Ni–Zn nanowire arrays. *J Magn Magn Mater*. 2009; 321:3511–3514.
4. Kim EH, Lee HS, Kwak BK, Kim B-K. Synthesis of ferrofluid with magnetic nanoparticles by sonochemical method for MRI contrast agent. *J Magn Magn Mater*. 2005;289:328–330.
5. Sun S, Murray CB. Synthesis of monodisperse cobalt nanocrystals and their assembly into magnetic superlattices. *J Appl Phys*. 1999; 85:4325–4330.
6. Allab F, Kedous-Lebouc A, Yonnet JP, Fournier JM. A magnetic field source system for magnetic refrigeration and its interaction with magnetocaloric material. *Int J Refrig*. 2006;29:1340–1347.
7. Kitanovski A, Egolf PW. Application of magnetic refrigeration and its assessment. *J Magn Magn Mater*. 2009;321:777–781.
8. Tartaj P, Morales MdP, Veintemillas-Verdaguer S, González-Carreño T, Serna CJ. The preparation of magnetic nanoparticles for applications in biomedicine. *J Phys D: Appl Phys*. 2003;36(13): R182.
9. Son SU, Jang Y, Park J, Na HB, Park HM, Yun HJ, Lee J, Hyeon T. Designed synthesis of atom-economical Pd/Ni bimetallic nanoparticle-based catalysts for sonogashira coupling reactions. *J Am Chem Soc*. 2004;126(16):5026–5027.
10. Ung D, Viau G, Ricolleau C, Warmont F, Gredin P, Fiévet F. CoNi nanowires synthesized by heterogeneous nucleation in liquid polyol. *Adv Mater*. 2005;17(3):338–344.
11. Soumare Y, Dakhlaoui-Omrani A, Schoenstein F, Mercone S, Viau G, Jouini N. Nickel nanofibers and nanowires: elaboration by reduction in polyol medium assisted by external magnetic field. *Solid State Commun*. 2011;151(4):284–288.
12. Batlle X, Labarta A. Finite-size effects in fine particles: magnetic and transport properties. *J Phys D: Appl Phys*. 2002;35(6):R15.
13. Gajbhiye NS, Sharma S, Ningthoujam RS. Synthesis of self-assembled monodisperse 3 nm FePd nanoparticles: phase transition, magnetic study, and surface effect. *J Appl Phys*. 2008;104(12): 123906.
14. Weller D, Moser A. Thermal effect limits in ultrahigh-density magnetic recording. *IEEE Trans Magn*. 1999;35(6):4423–4439.
15. Gajbhiye NS, Sharma S, Nigam AK, Ningthoujam RS. Tuning of single to multi-domain behavior for monodispersed ferromagnetic cobalt nanoparticles. *Chem Phys Lett*. 2008;466(4–6):181–185.
16. Maurer T, Ott F, Chaboussant G, Soumare Y, Piquemal JY, Viau G. Magnetic nanowires as permanent magnet materials. *Appl Phys Lett*. 2007;91(17):172501–172503.
17. Sun S, Murray CB, Weller D, Folks L, Moser A. Monodisperse FePt nanoparticles and ferromagnetic FePt nanocrystal superlattices. *Science*. 2000;287(5460):1989–1992.
18. Liu HL, Wu JH, Min JH, Kim YK. Synthesis of monosized magnetic-optical AuFe alloy nanoparticles. *J Appl Phys*. 2008; 103(7):07D529-521–507D529-523.
19. Tamada Y, Yamamoto S, Takano M, Nasu S, Ono T. Composition-dependent magnetic properties of FePt nanoparticles synthesized by the SiO2-nanoreactor method. *Phys Status Solidi C*. 2007;4(12): 4503–4506.
20. Dormann JL, Bessais L, Fiorani D. A dynamic study of small interacting particles: superparamagnetic model and spin-glass laws. *J Phys C: Solid State Phys*. 1988;21(10):2015–2034.
21. Ugarte D, Stöckli T, Bonard JM, Châtelain A, de Heer WA. Filling carbon nanotubes. *Appl Phys A*. 1998;67(1):101–105.
22. Figlarz M, Fiévet F, Lagier JP. *French patent, No*. 8,221,483. 1985.
23. Fiévet F, Brayner R. The polyol process. In: Brayner R, Fiévet F, Coradin T, editors. *Nanomaterials: A Danger or a Promise?* London: Springer, 2013:1–25.
24. Cha SI, Mo CB, Kim KT, Hong SH. Ferromagnetic cobalt nanodots, nanorices, nanowires and nanoflowers by polyol process. *J Mater Res*. 2005;20(08):2148–2153.
25. Ung D, Soumare Y, Chakroune N, Viau G, Vaulay MJ, Richard V, Fiévet F. Growth of magnetic nanowires and nanodumbbells in liquid polyol. *Chem Mater*. 2007;19(8):2084–2094.
26. Soumare Y, Piquemal JY, Maurer T, Ott F, Chaboussant G, Falqui A, Viau G. Oriented magnetic nanowires with high coercivity. *J Mater Chem*. 2008;18(46):5696–5702.
27. Soumare Y, Garcia C, Maurer T, Chaboussant G, Ott F, Fiévet F, Piquemal J-Y, Viau G. Kinetically controlled synthesis of hexagonally close-packed cobalt nanorods with high magnetic coercivity. *Adv Funct Mater*. 2009;19(12):1971–1977.
28. Viau G, Garcıa C, Maurer T, Chaboussant G, Ott F, Soumare Y, Piquemal JY. Highly crystalline cobalt nanowires with high coercivity prepared by soft chemistry. *Phys Status Solidi A*. 2009;206(4): 663–666.
29. Liu Q, Guo X, Wang T, Li Y, Shen W. Synthesis of CoNi nanowires by heterogeneous nucleation in polyol. *Mater Lett*. 2010; 64(11):1271–1274.
30. Ait Atmane K, Zighem F, Soumare Y, Ibrahim M, Boubekri R, Maurer T, Margueritat J, Piquemal J-Y, Ott F, Chaboussant G, Schoenstein F, Jouini N, Viau G. High temperature structural and magnetic properties of cobalt nanorods. *J Solid State Chem*. 2013; 197:297–303.
31. Sun Y, Xia Y. Large-scale synthesis of uniform silver nanowires through a soft, self-seeding, polyol process. *Nature*. 1991;353(1991): 737.
32. Coskun S, Aksoy B, Unalan HE. Polyol synthesis of silver nanowires: an extensive parametric study. *Cryst Growth Des* 2011; 11(11):4963–4969.
33. Chen J, Herricks T, Geissler M, Xia Y. Single-crystal nanowires of platinum can be synthesized by controlling the reaction rate of a polyol process. *J Am Chem Soc*. 2004;126(35):10854–10855.
34. Tsuji M, Hashimoto M, Nishizawa Y, Tsuji T. Synthesis of gold nanorods and nanowires by a microwave–polyol method. *Mater Lett*. 2004;58(17–18):2326–2330.
35. Korgel BA. Semiconductor nanowires: a chemical engineering perspective. *AIChE J*. 2009;55(4):842–848.

36. Paul EL, Atiemo-Obeng V, Kresta SM. *Handbook of Industrial Mixing: Science and Practice*: Wiley, New York, USA, 2004.
37. Karaagac O, Kockar H. Effect of synthesis parameters on the properties of superparamagnetic iron oxide nanoparticles. *J Supercond Novel Magn*. 2012;25(8):2777–2781.
38. Devaraj NK, Ong BH, Matsumoto M. Characterization of chemically prepared magnetite nanoparticles. *Synth React Inorg Met-Org Nano-Met Chem*. 2008;38(2):204–207.
39. Devaraj NK, Ong BH. Effects of calcination on the magnetic properties of iron oxide nanoparticles. *AIP Conf Proc*. 2011;1328(1):288–290.
40. Devaraj NK, Ong BH, Matsumoto M. Yield Control of chemically-synthesized magnetite nanoparticles. *Synth React Inorg Met-Org Nano-Met Chem*. 2008;38(2):208–211.
41. Lin R-Y, Dayananda K, Chen T-J, Chen C-Y, Liu G-C, Lin K-L, Wang Y-M. Targeted RGD nanoparticles for highly sensitive in vivo integrin receptor imaging. *Contrast Media Mol Imaging*. 2012;7(1): 7–18.
42. Sun J, Zhou S, Hou P, Yang Y, Weng J, Li X, Li M. Synthesis and characterization of biocompatible Fe3O4 nanoparticles. *J Biomed Mater Res Part A*. 2007;80A(2):333–341.
43. Hua CC, Zakaria S, Farahiyan R, Khong LT, Abdullah M, Ahmad S,Nguyen KL. Size-controlled synthesis and characterization of Fe3O4 nanoparticles by chemical coprecipitation method. *Sains Malaysiana*. 2008;37(4):389–394.
44. Mahdavi M, Ahmad M, Haron M, Namvar F, Nadi B, Rahman M, Amin J. Synthesis, surface modification and characterisation of biocompatible magnetic iron oxide nanoparticles for biomedical applications. *Molecules*. 2013;18(7):7533–7548.
45. Zauner R, Jones AG. On the influence of mixing on crystal precipitation processes—application of the segregated feed model. *Chem Eng Sci*. 2002;57(5):821–831.
46. Bałdyga J, Orciuch W. Barium sulphate precipitation in a pipe—an experimental study and CFD modelling. *Chem Eng Sci*. 2001;56(7): 2435–2444.
47. Falk L, Schaer E. A PDF modelling of precipitation reactors. *Chem Eng Sci*. 2001;56(7):2445–2457.
48. Jaworski Z, Nienow AW. CFD modelling of continuous precipitation of barium sulphate in a stirred tank. *Chem Eng J*. 2003;91(2–3):167–174.
49. Marchisio DL, Barresi AA, Garbero M. Nucleation, growth, and agglomeration in barium sulfate turbulent precipitation. *AIChE J*. 2002;48(9):2039–2050.
50. Rousseaux JM, Vial C, Muhr H, Plasari E. CFD simulation of precipitation in the sliding-surface mixing device. *Chem Eng Sci*. 2001; 56(4):1677–1685.
51. Wang L, Fox RO. Application of in situ adaptive tabulation to CFD simulation of nano-particle formation by reactive precipitation. *Chem Eng Sci*. 2003;58(19):4387–4401.
52. Wei H, Zhou W, Garside J. Computational fluid dynamics modeling of the precipitation process in a semibatch crystallizer. *Ind Eng Chem Res*. 2001;40(23):5255–5261.
53. Baldyga J, Podgórska W, Pohorecki R. Mixing-precipitation model with application to double feed semibatch precipitation. *Chem Eng Sci*. 1995;50(8):1281–1300.
54. Barresi AA, Marchisio D, Baldi G. On the role of micro- and meso-mixing in a continuous Couette-type precipitator. *Chem Eng Sci*. 1999;54(13–14):2339–2349.
55. Johnson BK, Prud'homme RK. Flash nanoprecipitation of organic actives and block copolymers using a confined impinging jets mixer. *Aust J Chem*. 2003;56(10):1021–1024.
56. Schwarzer H-C, Schwertfirm F, Manhart M, Schmid H-J, Peukert W. Predictive simulation of nanoparticle precipitation based on the population balance equation. *Chem Eng Sci*. 2006;61(1):167–181.
57. Johnson BK, Prud'homme RK. Chemical processing and micromixing in confined impinging jets. *AIChE J*. 2003;49(9):2264–2282.
58. Di Pasquale N, Marchisio DL, Barresi AA. Model validation for precipitation in solvent-displacement processes. *Chem Eng Sci*. 2012; 84:671–683.
59. Cheng JC, Fox RO. Kinetic modeling of nanoprecipitation using CFD coupled with a population balance. *Ind Eng Chem Res*. 2010; 49(21):10651–10662.
60. Favero JL, Silva LFLR, Lage PLC. Comparison of methods for multivariate moment inversion—introducing the independent component analysis. *Comput Chem Eng*. 2014;60:41–56.
61. Bockhorn H, Mewes D, Peukert W, Warnecke H-J. *Micro and Macro Mixing Analysis, Simulation and Numerical Calculation*: Springer-Verlag, Berlin, Germany, 2010.
62. Marmo L, Manna L, Chiampo F, Sicardi S, Bersano G. Influence of mixing on the particle size distribution of an organic precipitate. *J Cryst Growth*. 1996;166(1–4):1027–1034.
63. Mahajan AJ, Kirwan DJ. Micromixing effects in a two-impinging-jets precipitator. *AIChE J*. 1996;42(7):1801–1814.
64. Santillo G, Deorsola FA, Bensaid S, Russo N, Fino D. MoS2 nanoparticle precipitation in turbulent micromixers. *Chem Eng J* 2012; 207–208:322–328.
65. Winkelmann M, Schuler T, Uzunogullari P, Winkler CA, Gerlinger W, Sachweh B, Schuchmann HP. Influence of mixing on the precipitation of zinc oxide nanoparticles with the miniemulsion technique. *Chem Eng Sci*. 2012;81:209–219.
66. Bensaid S, Deorsola FA, Marchisio DL, Russo N, Fino D. Flow field simulation and mixing efficiency assessment of the multi-inlet vortex mixer for molybdenum sulfide nanoparticle precipitation. *Chem Eng J*. 2014;238:66–77.
67. Scherrer P. Bestimmung der Grösse und der inneren Struktur von Kolloidteilchen mittels Röntgenstrahlen. *Nachrichten von der Gesellschaft der Wissenschaften zu Göttingen, Mathematisch-Physikalische Klasse* 1918;26:98–100.
68. Langford JI, Wilson AJC. Scherrer after sixty years: a survey and some new results in the determination of crystallite size. *J Appl Crystallogr*. 1978;11(2):102–113.
69. Ricolleau C, Nelayah J, Oikawa T, Kohno Y, Braidy N, Wang G, Hue F, Florea L, Pierron-Bohnes V, Alloyeau D. Performances of an 80–200 kV microscope employing a cold-FEG and an aberration-corrected objective lens *Microscopy (Oxf)*. 2013;62(2): 283–293.
70. Qian R-Y, Chen Z-D, Ni H-G, Fan Z-Z, Cai F-D. Crystallization kinetics of potassium chloride from brine and scale-up criterion. *AIChE J*. 1987;33(10):1690–1697.
71. Zlokarnik M. *Dimensional Analysis and Scale-Up in Chemical Engineering*: Springer-Verlag, Berlin, Germany, 1991.
72. Ouar N, Bousnina MA, Schoenstein F, Mercone S, Brinza O, Farhat S, Jouini N. Spark plasma sintering of Co80Ni20 nanopowders synthesized by polyol process and their magnetic and mechanical properties. *J Alloys Compd*. In press.
73. Ung D, Viau G, Fiévet-Vincent F, Herbst F, Richard V, Fiévet F. Magnetic nanoparticles with hybrid shape. *Prog Solid State Chem*. 2005;33(2–4):137–145.
74. Ouar N, Schoenstein F, Mercone S, Farhat S, Villeroy B, Leridon B, Jouini N. Spark-plasma-sintering magnetic field assisted compaction of Co80Ni20 nanowires for anisotropic ferromagnetic bulk materials. *J Appl Phys*. 2013;114(16):163907.
75. Ott F, Maurer T, Chaboussant G, Soumare Y, Piquemal J-Y, Viau G. Effects of the shape of elongated magnetic particles on the coercive field. *J Appl Phys*. 2009;105(1):013915.
76. Brandenburg K, Putz H. Match: Phase identification from powder diffraction. User Manual, version 1.9, by Crystal IMPACT, Germany. Copyright © 2003–2009.
77. Maurer T, Zighem F, Ott F, Chaboussant G, André G, Soumare Y, Piquemal J-Y, Viau G, Gatel C. Exchange bias in Co/CoO core-shell nanowires: role of antiferromagnetic superparamagnetic fluctuations. *Phys Rev B*. 2009;80(6):064427.
78. Fischbacher T, Franchin M, Bordignon G, Fangohr H. A systematic approach to multiphysics extensions of finite-element-based micromagnetic simulations: Nmag. *IEEE Trans Magn*. 2007;43(6):2896–2898.
79. Zighem F, Maurer T, Ott F, Chaboussant G. Dipolar interactions in arrays of ferromagnetic nanowires: a micromagnetic study. *J Appl Phys*. 2011;109(1):013910.
80. ANSYS, Inc. (2010, November). ANSYS Workbench User's Guide. Canonsburg, Pennsylvania, United States of America.

Manuscript received May 2, 2014, and revision received Aug. 1, 2014.